

# Millimeter-Wave Massive MU-MIMO Performance Analysis for Private Underground Mine Communications

Saif Eddine Hadji<sup>1</sup>, Member, IEEE, Mourad Nedil<sup>1</sup>, Senior Member, IEEE, Mohamed Lamine Seddiki<sup>1</sup>, and Ismail Ben Mabrouk<sup>1</sup>, Senior Member, IEEE

**Abstract**—In this article, a performance analysis of millimeter wave (mmWave) massive multiuser multiple-input and multiple-output (MU-MIMO) channel within an underground mine is performed. The analysis is based on channel measurements conducted at 28 GHz using a base station of 64 virtual antenna elements serving multiple users. Channel characteristics such as large-scale path loss, time dispersion, coherence bandwidth and sum-rate capacity are reported and evaluated. The results indicate that multislope path loss model is better suited for precise prediction of path loss across various propagation segments within the mining gallery. The time dispersion analysis reveals that the underground mine channel does not cause significant time dispersion, as 90% of the root-mean-square (rms) delay spreads are below 4 ns. In addition, it was found that the rms delay spread is not dependent on the propagation distance. The study on sum-rate capacity highlights the potential of employing massive MIMO technology to improve the channel's spectral efficiency. The analysis reveals that the capacity, with eight active users, can reach up to 33.54 bit/s/Hz. The outcomes of this article offer valuable insights into the propagation properties of underground mine environment, which is characterized by rich-scattering and irregular topology.

**Index Terms**—5G, 28 GHz, channel capacity, channel measurements, massive multiuser multiple input and multiple output (MU-MIMO), millimeter-wave (mmWave), path loss, root-mean-square (rms) delay spread, underground mine.

## I. INTRODUCTION

**M**INE 4.0 or smart mine is the name that is generally given to the mine which adopts the characteristics specific to the fourth industrial revolution (Industry 4.0) [1]. To improve safety and productivity, mining companies are rapidly deploying new tools and technologies including telemetry, wireless sensors, and remote mining. Mining 4.0 makes use of technologies such as the fifth-generation mobile network (5G), Internet of Things (IoT) sensing, artificial intelligence (AI), and machine learning [2]. Nowadays, most of mining companies are planning to invest in wireless

infrastructure and most of them named the private (nonpublic) 5G networks as their priority [3]. It is anticipated to provide ultrahigh data rates in the multi-Gb/s range, along with sub-millisecond latency. This will enable operation of autonomous vehicles, real-time status tracking of equipment and miners, remote diagnostic and maintenance, and facilitate the connection of hundreds of thousands of IoT sensors and devices, both on surface and underground [4].

Compared to conventional residential, commercial, and industrial indoor environments, establishing fully flexible and high-speed reliable networks face unique propagation challenges in underground mine which require innovative solutions. Underground mining environments are known for having walls with extremely rough surfaces, confined space, and an expanding network of tunnels and galleries, which make network planning, and deployment more challenging [5]. Therefore, a precise channel characterization based on realistic measurements is necessary to design an efficient 5G wireless communication network for underground mines.

The implementation of industrial 5G systems will require significant improvements in terms of transmission bandwidth, which can be achieved by utilizing new bands at higher frequencies [6]. Hence, mmWave spectrum is one key enabling solution for meeting the enormous increase in channel capacity demand [7]. However, millimeter-wave (mmWave) channels are strongly sensitive to environment dimensions, presence of physical obstacles and scatterers [8], [9]. These higher frequencies often experience significant path loss and require a clear line of sight (LOS) between the transmitter and receiver. Therefore, massive multiple-input and multiple-output (MIMO) techniques have the capability to address these challenges and greatly improve the spectral efficiency [10]. The combination of mmWave and massive MIMO is expected to drastically enhance the wireless network performance, by bringing together the huge available mmWave bandwidth and the expected gain of massive MIMO arrays, making them the best solutions for 5G systems [11].

While the challenges confronting mmWave and massive MIMO applications in underground mine environments are substantial, including high signal attenuation, the complex 3-D nature of mines with limited direct links, multipath interference undermining signal integrity, potential signal blockage due to machinery and infrastructure, the precision required for beamforming alignment, and potential interference

Manuscript received 29 April 2023; revised 1 October 2023; accepted 3 November 2023. Date of publication 13 December 2023; date of current version 15 February 2024. This work was supported by Fonds de recherche du Québec Nature et technologies (FRQNT). (Corresponding author: Saif Eddine Hadji.)

Saif Eddine Hadji, Mourad Nedil, and Mohamed Lamine Seddiki are with the School of Engineering, University of Quebec in Abitibi Témiscamingue, Val-d'Or, QC J9P 1Y3, Canada (e-mail: saifeddine.hadji@uqat.ca).

Ismail Ben Mabrouk is with the Department of Engineering, Durham University, DH1 3LE Durham, U.K.

Color versions of one or more figures in this article are available at <https://doi.org/10.1109/TAP.2023.3340301>.

Digital Object Identifier 10.1109/TAP.2023.3340301

from neighboring communication systems. Nevertheless, the adoption of mmWave and massive MIMO technologies in underground mine wireless communications offers a multitude of advantages. Beyond the high data rates and low latency benefits, these technologies excel in enhancing signal quality through precise signal direction, effectively addressing multipath effects and interference. Moreover, the utilization of directional beamforming optimizes coverage over extended tunnel distances, minimizing signal attenuation compared to omnidirectional propagation. The adaptability of mmWave and Massive MIMO systems to the tunnel's unique geometry further helps in optimizing coverage while mitigating signal blockage challenges. By reducing interference through directional propagation and beamforming, these technologies ensure more reliable and consistent communication links.

Recently, several studies have reported experimental measurement at mmWave frequency bands, such as 28, 38, 60, and 73 GHz [6], [7], [8], [12], [13], [14], [15], [16], [17], [18], [19], [20], [21], [22], [23], [24], [25], [26], [27], [28]. Different measurement campaigns have been carried out in various tunnel-like environments, such as pedestrian tunnels [24], airport terminals [25], [26], railway stations [27], office environments [8], and subway tunnels [18], [21]. However, mmWave propagation in underground mines is relatively scarce in the literature. Previous research studies on mmWave in underground mine environments are limited to 60 GHz. In [28], a measurement campaign was performed at 60 GHz to characterize a  $2 \times 2$  MIMO channel in an underground mine using a patch antenna. The authors focused on extracting statistical parameters of the propagation channel, such as PL, rms delay spread, Rician K-factor, channel correlation, and capacity. In [16], single-input single-output (SISO) measurements were also conducted at 60 GHz in two different underground mining galleries. The performance of the LOS link in terms of path loss exponent (PLE) and capacity have also been studied. The results show that the PLE in the underground mine gallery is found to be lower than the free space value and the channel capacity in a narrow tunnel is higher than in a wider one. Ghaddar et al. [17] have also performed a similar measurement campaign at 60 GHz in which they have compared the performance of directional SISO propagation with  $2 \times 2$  directional MIMO. The study reveals that the proposed directional MIMO has a greater ability to overcome the effect of miners' body obstruction. However, the maximum measured distance in the aforementioned studies was limited to 10 m due to constraints in the measurement setup. At such short distances, the propagation occurs as it were in free space, without the manifestation of the waveguiding effect. Consequently, the underground mine channel has no significant impact on signal propagation.

Despite the interest that attracts massive MIMO systems at mmWaves among the research community, only few studies in tunnel-like environments have been reported. In [20], [29], and [30], MIMO channel characteristics are investigated in a subway-like short tunnel at 28-GHz frequency band. Statistical parameters such as rms delay spread, K-factor, and shadowing were studied. These works only employed a channel bandwidth of 100 MHz and did not include any

path loss examination. Another measurement campaigns have been conducted at 25–40 GHz inside an underground convoy in Spain [31], [32]. In these works, MU-MIMO channel propagation characteristics in an intra-wagon environment were presented. However, the environment exhibits distinct characteristics that are different from those observed in an underground mining gallery.

To the best of the authors knowledge, this article presents the first reported experimental investigation of wideband mmWave massive MU-MIMO channel in an underground mining environment. The measurement campaign was conducted at 28 GHz with a bandwidth of 800 MHz, utilizing broadband radio over fiber (RfOF) link to allow long-distance measurements. A comprehensive performance analysis of the channel was conducted, with a particular focus on large-scale path loss, temporal dispersion, frequency selectivity, singular value spread (SVS), and sum-rate capacity. The findings were compared and assessed, offering valuable insights into the propagation characteristics in this challenging environment.

The remainder of the paper is organized the following way. The experimental setup, environment description, and measurement procedure are presented in Section II. Section III presents path loss results and models. Section IV provides the measured rms delay spread and coherence bandwidth. Section V includes the results of the SVS as well as the sum-rate capacity. Conclusions are drawn in Section V.

## II. MEASUREMENT SETUP AND ENVIRONMENT

To characterize the mmWave Massive MU-MIMO channel in an underground mine, wideband measurements were conducted at 28 GHz using frequency-domain channel sounding. The 28 GHz band is among the most important bands in mmWave communication according to the regulations of 3GPP and ITU WRC-15 [33]. Recently, the 3GPP band n257 (27.5–28.35 GHz) was adopted to support the millimeter-wave spectrum in Canada and USA [34]. It is worth mentioning that this potential candidate band is still unexplored in underground mine environments.

### A. Underground Mine Description

The measurement campaign was performed in the Old Lamaque mine which is a former gold mine located in Val D'or, QC, Canada. An underground gallery at a depth of 91 m was exploited to carry out propagation measurements. This gallery has a downward slope of approximately 20% over 50 m serving as a connecting tunnel between the auditorium and a lower level. Beyond this point, the tunnel extends horizontally for 150 m with several curves along the way. The gallery consists of an arched ceiling tunnel with a mean width of 3.8 m and a mean height of 2.8 m. The walls are very rough and consist of sharp edges. The humidity level can reach 100% and the temperature is about 8 °C. The gallery is equipped with a roof bolting system that consists of metallic rods and nets. Fig. 1 shows the plan layout of the mining gallery.

### B. Experimental Setup

The experimental setup used in this measurement campaign is illustrated in Fig. 2. The measurement system is based

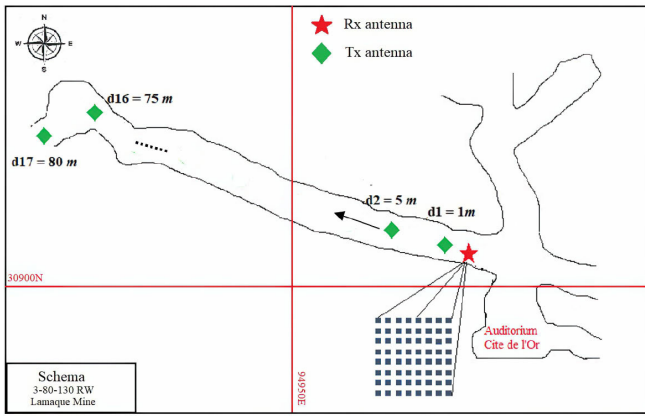


Fig. 1. Mining gallery plan layout.

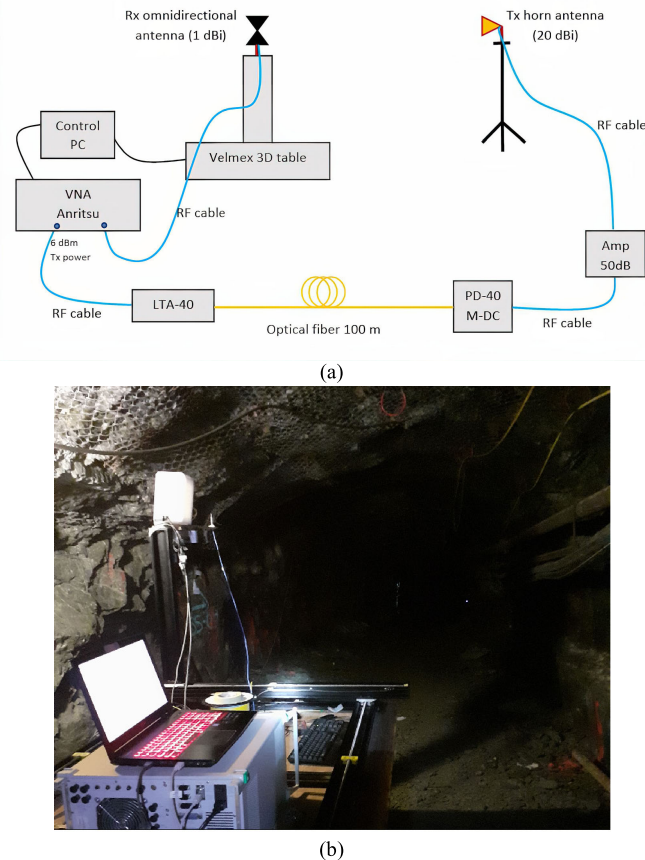


Fig. 2. (a) Schematic of the channel sounder and (b) photograph of the measurement setup.

on the frequency domain channel sounding method. The system mainly consisted of a vector network analyzer (VNA) Anritsu MS4647A, that operates from 10 MHz to 70 GHz, to measure the forward transmission coefficient  $S_{21}(f)$  of the wireless channel, equivalent to the complex channel transfer function (CTF)  $H(f)$  [35]. In addition, the Anritsu MS4647A offers a time domain option by transforming the frequency response, using the chirp z inverse fast Fourier transform, into the time domain which is equivalent to the channel impulse response (CIR)  $h(t)$  [36]. Omnidirectional antenna

(gain of 1 dBi) was used at the receiver (Rx) side during the measurement campaigns. For the transmitter (Tx) side, a waveguide horn antenna (gain of 20 dBi) was employed due to its capability of directing a significant portion of the transmitted power toward the mine gallery, thereby enhancing the waveguide effect [37].

The main drawback of using channel sounder-based VNA is the limitation of range and mobility due to the high attenuation by RF cables, especially at mmWave frequencies. To address this issue, a broadband RfOf link (by Optilab) is considered to connect the Tx antenna to the VNA. This part of the setup consists of a high-performance lightwave transmitter module (LTA-40) connected to a bandwidth PIN receiver module (PD-40-M-dc) through a single-mode fiber, operating from dc to 40 GHz. Hence, the low attenuation of the optical fiber (1.5 dB/km) allows for improving the dynamic range of the sounder which could extend the measurement range from few meters to several hundreds of meters. In addition, an amplifier (gain of 50 dB) is also connected to the Tx antenna to compensate for the losses introduced by the RfOf link before transmission [38].

The Rx antenna has been mounted on a 3-D motion control positioning system from Velmex, Inc., which allows vertical planar scanning to form a virtual uniform rectangular array (URA). The 3-D positioning system and the VNA were both remotely controlled using a personal computer (PC) via serial cables (RS 232 and USB type B). A developed LabVIEW application was also used to simultaneously control the movement of the 3-D positioning system and to perform real-time data acquisition from the VNA.

### C. Measurement Procedure

The maximum RF transmit power was fixed at 6 dBm over the 800 MHz bandwidth. The number of sweep points was set to 1201 which corresponds to a maximum excess delay of  $1.5 \mu\text{s}$ . Since the VNA takes time to sweep over the measured frequency bands, there were no moving people or objects in the gallery, leading to a static channel. To emulate an uplink massive MU-MIMO system, the Rx subsystem which is considered as a base station (BS), was placed close to the left side wall of the gallery at a height of 1.7 m to form a virtual URA of 64 elements uniformly spaced by  $\lambda/2$  and perpendicular to the gallery wall. At the Tx side, the horn antenna was fixed on a tripod with a height of 1.6 m to emulate an active user equipment (UE). A total of 17 different locations were predefined on the mine gallery of which 12 of them are related to LOS links (Tx1–Tx13), and the rest are referred to nonline of sight (NLOS), as illustrated in Fig. 1. The Tx horn antenna was aligned (using laser beam tool) to the center of the Rx URA, for all locations, to achieve the maximum received power. For each Tx–Rx combination, the CTF and the CIR were recorded providing a total of 2176 measurements. Finally, Table I summarizes the main parameters regarding the measurement settings.

It is worth mentioning that before the measurement campaign, the VNA is first calibrated using Short-Open-Load-Thru (SOLT) technique to remove the effect of RF cables and other passive elements in the measurement system.

TABLE I  
MEASUREMENT SETTINGS AND SPECIFICATION

Center frequency	28 GHz
Bandwidth	800 MHz
Tx Antenna gain	20 dBi
Rx Antenna gain	1 dBi
Antenna polariz.	V-V
Trans. Power	6 dBm
Sweep points	1201
Tx Height	1.6 m
Rx Height	1.7 m

The CTF  $H(f)$  can be derived from the measured transmission parameter  $S_{21}(f)$  which can be expressed in the frequency domain as follows:

$$S_{21}(f) = H(f)H_{\text{sys}}(f) \quad (1)$$

where  $H_{\text{sys}}(f)$  is the transfer function of the Tx and Rx link.

To measure the impact of the equipment (RFoF link, fiber, and amplifier), reference measurements at 1-m separation distance have been conducted in an anechoic chamber. The measured  $S_{21\text{ref}}(f)$  parameter can be expressed as follows:

$$S_{21\text{ref}}(f) = H_{\text{ref}}(f)H_{\text{sys}}(f). \quad (2)$$

Then, the transfer function of the Tx and Rx link equipment can be determined as follows:

$$H_{\text{sys}}(f) = \frac{S_{21\text{ref}}(f)}{H_{\text{ref}}(f)} \quad (3)$$

where  $H_{\text{ref}}(f)$  is the free space transfer function.

### III. PATH LOSS MODELS

#### A. Path Loss Measurement

Path loss denotes the signal power loss in the propagation channel and is used to determine link budgets by evaluating the propagation loss between the transmitter and the receiver. As a result, the path loss values are frequency-dependent rather than antenna gain or transmitted power level. The local wideband path loss can be extracted from the measured CTF as follows [35]:

$$PL = \frac{1}{N_f} \sum_{k=1}^{N_f} |H(f_k)|^2 \quad (4)$$

where  $N_f$  is the number of sweep points.

According to the calibration mentioned above, the CTF can be expressed as follows:

$$H(f_k) = \frac{S_{21}(f_k)}{H_{\text{sys}}(f_k)}. \quad (5)$$

Finally, the wideband path loss can be obtained using the following expression:

$$PL(\text{dB}) = -10 \log_{10} \left( \frac{1}{N_f} \sum_{k=1}^{N_f} \left| \frac{S_{21}(f_k)}{H_{\text{sys}}(f_k)} \right|^2 \right). \quad (6)$$

#### B. Path Loss Modeling

Large-scale path loss models are important in designing communication systems [8]. They are used to predict link budgets by estimating the attenuation over the distance of propagating signals. Among different types of large-scale channel models (empirical, stochastic, and deterministic), path loss models based on measurements offer a realistic insight into propagation characteristics [8]. Thus, two potential path loss models (log-distance and multislope) have been considered in this study.

The log-distance path loss model is widely used in wireless communications because it provides a simple and practical way to predict the received signal strength [39]. Hence, the log-distance path loss model can be used to estimate the large-scale fading resulting from multimode propagation in the underground mine [40]. This model is parametrized by PLE parameter  $n$ , and it is given by the following equation [40]:

$$PL[\text{dB}] = PL_0[\text{dB}] + 10n \log_{10} \left( \frac{d}{d_0} \right) + \chi_\sigma \quad (7)$$

where  $PL_0$  is the path loss at a reference distance  $d_0$  (generally taken as 1 m),  $d$  is the Tx–Rx separation distance in meters, and  $\chi_\sigma$  is a zero mean Gaussian random variable with a standard deviation  $\sigma$  in dB.

In fact, the propagation in the mine gallery is based on the hypothesis that propagation takes the form of waveguide transmission [41]. Therefore, in the LOS scenario, the signal undergoes free space propagation in the near region. Then, a lower attenuation is shown after a particular distance known as the breakpoint distance  $d_{\text{bp}}$  [42]. At the end of the LOS segment, the signal encounters a higher attenuation in the NLOS segment between 60 and 80 m. As a result, a multislope path loss model is proposed for a better modeling of the wave propagation in the underground mining gallery. In a typical indoor and outdoor environment, separate path loss models are used for LOS and NLOS scenarios. However, in tunnel propagation, a more effective approach is to combine these path loss models into a single multislope path loss model [43] and [44]. The multislope path loss model is given by

$$PL[\text{dB}] = \begin{cases} PL_0 + 10n_1 \log_{10} \left( \frac{d}{d_0} \right) + \chi_{\sigma_1}, & \text{for } d \leq d_{\text{bp}} \\ PL_{\text{bp}} + 10n_2 \log_{10} \left( \frac{d}{d_{\text{bp}}} \right) + \chi_{\sigma_2}, & \text{for } d_{\text{bp}} \leq d \leq d_{\text{LOS}} \\ PL_{\text{LOS}} + 10n_3 \log_{10} \left( \frac{d}{d_{\text{LOS}}} \right) + \chi_{\sigma_3}, & \text{for } d \geq d_{\text{LOS}} \end{cases} \quad (8)$$

where  $PL_{\text{bp}}$  is the path loss at the breakpoint distance  $d_{\text{bp}}$ ,  $PL_{\text{LOS}}$  is the path loss at the maximum LOS distance ( $d_{\text{LOS}} = 60$  m),  $n_1$ ,  $n_2$  and  $n_3$  are the PLEs,  $\chi_{\sigma_1}$ ,  $\chi_{\sigma_2}$ , and  $\chi_{\sigma_3}$  are zero mean Gaussian variables with standard deviation of  $\sigma_1$ ,  $\sigma_2$ , and  $\sigma_3$ , respectively.

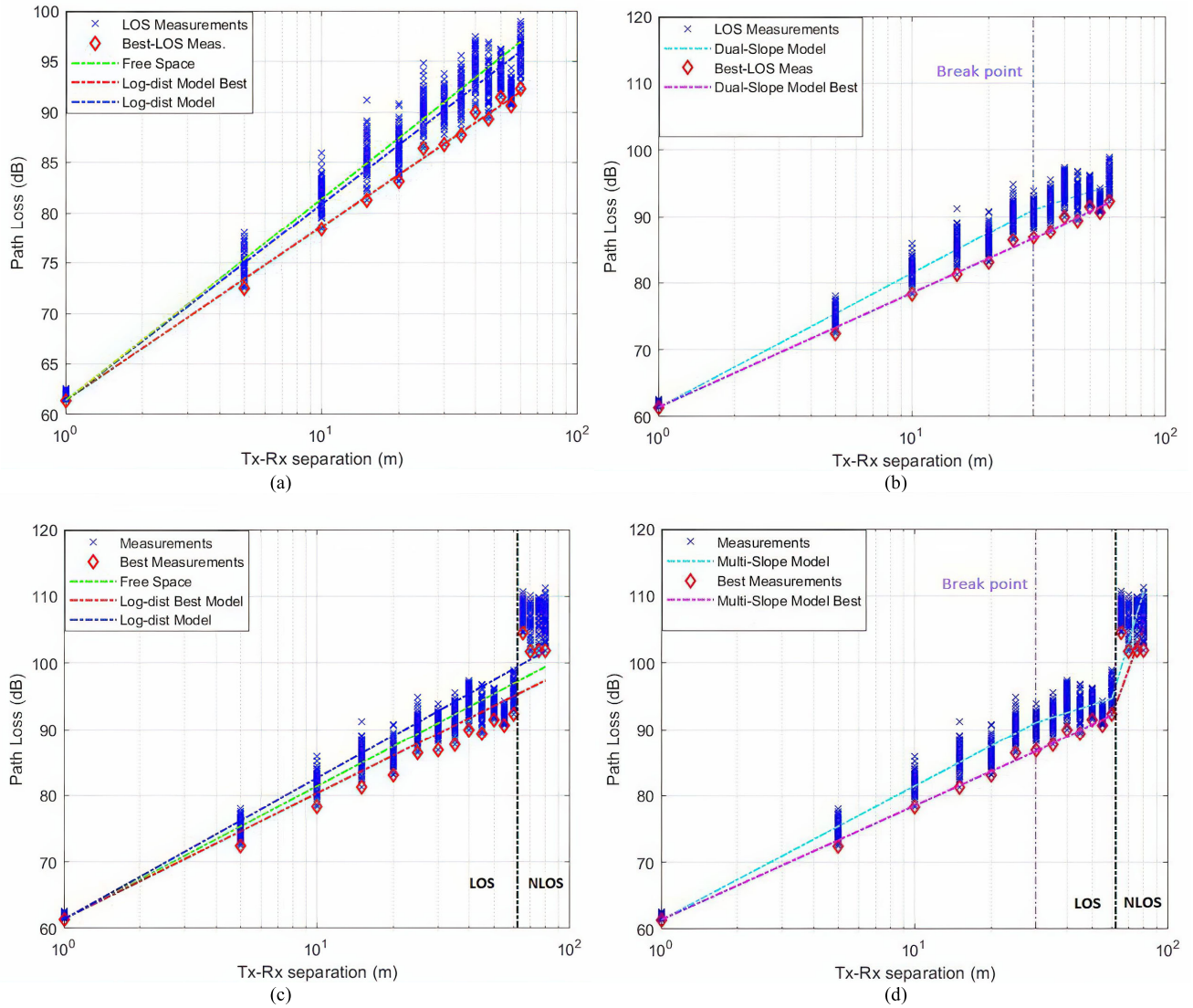


Fig. 3. Path Loss results: (a) log-distance path loss models for LOS measurements; (b) dual-slope path loss model for LOS measurements; (c) log-distance path loss models for LOS and NLOS measurements; and (d) multislope path loss model for LOS and NLOS measurements.

The breakpoint distance is determined based on measurements by averaging the path loss at each Tx location. Then, the breakpoint is identified as the point where the path loss consistently becomes lower than the free space path loss, while maintaining this differential criterion for successive positions.

Fig. 3(a) and (b) shows the path loss results in the LOS segment, while Fig. 3(c) and (d) illustrates the path loss results for the entire mining gallery, including two distinct segments: LOS and NLOS. Within these segments, we distinguish measurements based on received power. Specifically, measurements with the strongest received power in the LOS segment are referred to as “Best LOS measurements,” while those with the strongest received power in both LOS and NLOS segments are denoted as “Best Measurements” (Best Meas.). Fig. 3(a) shows the LOS measurements and Best LOS measurements, both fit with the log-distance path loss model. Meanwhile, Fig. 3(b) illustrates the LOS and Best-LOS measurements fit with the multislope model, with a focus on its unique dual-slope characteristics. To comprehensively assess the path loss in both LOS and NLOS scenarios, Fig. 3(c) and (d)

TABLE II  
PARAMETERS OF PATH LOSS MODELS

Model	Data	$n$	$\sigma$ (dB)				
Log-distance	Best LOS	1.72	0.62				
	LOS	1.95	1.97				
Log-distance	Best Meas.	1.89	3.68				
	LOS+NLOS	2.12	4.15				
Dual-slope		$n1$	$n2$	$\sigma1$	$\sigma2$		
	Best LOS	1.7	1.84	0.57	0.62		
	LOS	2	1.2	1.71	1.86		
Multi-Slope		$n1$	$n2$	$n3$	$\sigma1$	$\sigma2$	$\sigma3$
	Best Meas.	1.7	1.84	10.45	0.57	0.62	4.33
LOS+NLOS	Meas.	2	1.2	12.87	1.71	1.86	4.67

provides an overview of the path loss measurements and Best Measurements, paired with the log-distance and multislope models, respectively.

Table II summarizes the empirical values of the PLE and the shadow fading standard deviation. In the LOS scenario, both log-distance and dual-slope path loss models show a

good prediction of the channel, as the PLEs are less than the theoretical free space PLE of 2, which confirms the waveguiding effect of the underground mining gallery. However, the Dual-slope model provides a better fit for the LOS measurements. Prior to the breakpoint, the PLE  $n_1$  was equal to 2, which proves that the free-space propagation mechanism was established in the near region. Following the breakpoint, the propagation in the mine gallery was guided by fundamental modes, resulting in minimal fading and reduced loss, with a corresponding PLE value of  $n_1 = 1.2$ . In the Best-LOS scenario, the results show that the Dual-Slope path loss model does not provide any significant enhancement in fitting, making the Log-distance path loss model a more suitable choice due to its simplicity.

For the LOS and NLOS scenario, the log-distance model exhibits a PLE of 1.89 in the Best-measurement case, suggesting the presence of a waveguiding effect which does not match with the NLOS segment higher attenuation. Moreover, upon analysis of all measurements, the log-distance path loss model was found to have a PLE of 2.12, surpassing that of free space propagation and failing to capture the waveguiding effect in the LOS segment of the gallery. This result suggests that the log-distance model is inadequate in accurately modeling wave propagation in underground mine galleries that contain curved segments. This highlights the limitations of the log-distance model in capturing the complex propagation characteristics of such environments. On the other hand, the multislope model fits well the measurements. It shows that after the breakpoint distance, the multipath components propagate in the axial direction of the mine gallery and through reflections between the tunnel walls, resulting in a smaller propagation loss ( $n_2 = 1.2$ ). In the NLOS scenario, when the curved walls of the tunnel occlude the direct path, the waveguiding effect is weakened, causing an increase in the path loss in which the PLE  $n_3$  is equal to 10.45 and 12.87 for the Best-measurements and all measurements scenarios, respectively. These PLEs are in good agreement with those reported in similar studies conducted in curved tunnel [43]. Consequently, the multislope path loss model provides a better fit than the log-distance path loss model which makes it more accurate for determining the mmWave radio link budget in underground mining galleries.

The characteristic of waveguided propagation in underground mine gallery improves the received signal power at 28-GHz frequency, offering significant advantages for long-distance communication while reducing the need for extensive communications infrastructure. This characteristic is particularly valuable in excavation areas, where frequent blasting poses a risk to nearby network infrastructure, such as antennas and cabling. These practical considerations underscore the significance of the path loss measurements and models in optimizing communication for underground mining environments. Furthermore, the applicability of the path loss models discussed in this work extends beyond the specific mining environment under study. Three key approaches for generalization are proposed: First, empirical model parameters can be adjusted to match the unique characteristics of the target environment, enhancing predictive accuracy. Second, deterministic models like ray tracing can be refined using the

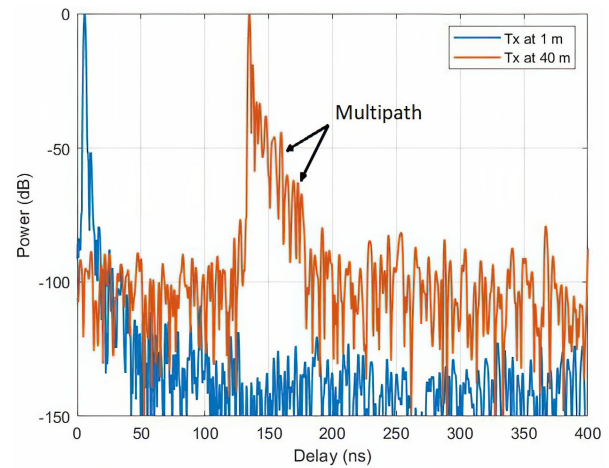


Fig. 4. Normalized PDPs measured from Rx25 at 1 and 40 m.

measurements as benchmarks to ensure predictions align with empirical findings, enabling extrapolation to other mining contexts. Lastly, the measurements can serve as valuable datasets for training artificial intelligence models, allowing them to predict path loss and signal strength in diverse environments.

#### IV. TEMPORAL DISPERSION AND FREQUENCY SELECTIVITY

##### A. rms Delay Spread

rms delay spread is a channel characteristic that is used to quantify the time dispersion properties of the wideband channels. Depending on the signal's bandwidth, the rms delay spread is considered as an indicator that can well describe the multipath time dispersion, the coherence bandwidth of the channel, as well as the severity of the inter-symbol interference [45]. The rms delay spread is mainly calculated using the power delay profile (PDP) function [45]. Moreover, the channel autocorrelation and frequency selectivity are highly dependent on the PDP. Fig. 4 shows two normalized PDPs measured at the Rx element number 25 at a Tx distance of 1 and 40 m, respectively.

By using the measured CIR, the PDP can be expressed as follows:

$$P(\tau_k) = |h(\tau_k)|^2. \quad (9)$$

The rms delay spread is defined as the square root of the second moment of the PDP [46]

$$\tau_{\text{rms}} = \sqrt{\frac{\sum_k P(\tau_k)\tau_k^2}{\sum_k P(\tau_k)} - \left(\frac{\sum_k P(\tau_k)\tau_k}{\sum_k P(\tau_k)}\right)^2} \quad (10)$$

where  $\tau_k$  is the  $k$ th excess delay time.

Fig. 5 displays the rms delay spread measured for each Tx–Rx position along the mine gallery. The boxes in the figure correspond to the interquartile range of the data, where the top and bottom of the box represent the 75% and 25% percentiles, respectively, where the whiskers extend to the farthest data points within the range. The rms delay spread values are observed to be highly consistent across most of the Tx positions, with relatively small dispersion. Interestingly, there is no

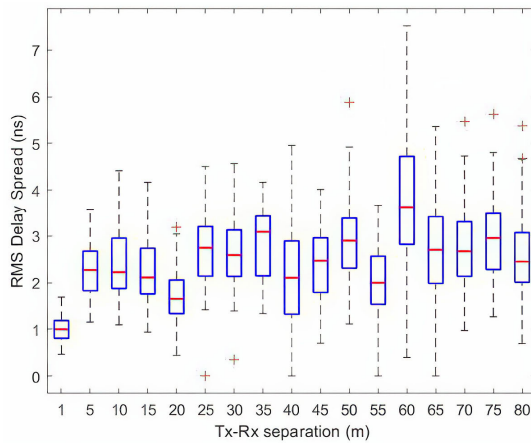


Fig. 5. rms delay spread in terms of Tx–Rx separation distance.

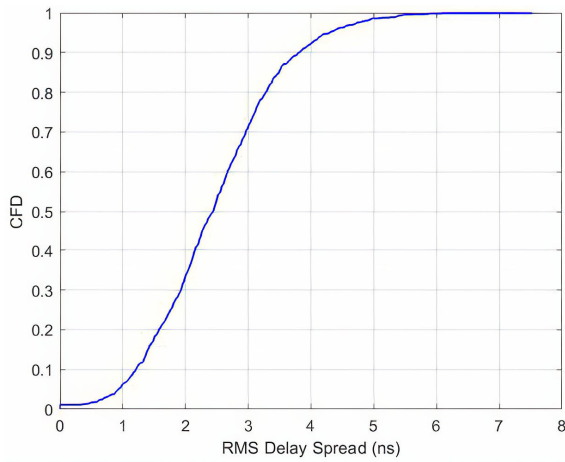


Fig. 6. cdf of the rms delay spread.

clear correlation between the propagation distance and the rms delay spread, which can be attributed to the waveguide effect observed within the gallery. Due to this effect, different paths cross similar distances by undergoing consecutive reflections on the gallery walls. Additionally, the high-order rays are highly attenuated due to multiple reflections and scattering on the rough walls, particularly for the mmWave band. Thus, the underground mine gallery does not cause a significant temporal dispersion which leads to a higher signal quality and lower error rates in data transmission.

At the specific 60-m separation distance, the variation in rms delay spread is more dispersed compared to the other positions. The values range from a minimum of 0.4 ns to a maximum of 7.52 ns. This dispersion is mainly caused by the presence of multipaths due to the earlier signal reflections caused by the changes in tunnel slope at 50 m. These earlier reflections occur on the floor and the ceiling edge, resulting in a higher chance of multipath effect compared to preceding distances. These multipaths are then collected by certain elements of the antenna array at the reception which explain the dispersion of the rms delay spread.

Fig. 6 shows the cumulative distribution function (cdf) of the rms delay spread over all Tx–Rx combinations. The cdf shows that 90% of the measured rms delay spreads are below 4 ns,

with a maximum measured value of 7.52 ns. These results are in good agreement with the reported values in [20], [47], and [48] obtained in similar environments.

### B. Coherence Bandwidth

The temporal dispersion caused by the channel produces a frequency selective behavior that can be described in terms of the autocorrelation function for a wide sense stationary uncorrelated scattering (WSSUS) channel [49]. The frequency correlation function can be obtained by considering the Fourier transform of the PDP [35] and it is given by

$$R_{\text{HH}}(q) = \sum_{n=0}^{N_f-1} |h(n)|^2 \exp\left(j \frac{2\pi}{N_f} nq\right). \quad (11)$$

The coherence bandwidth ( $B_c$ ) is defined as the frequency range at which the normalized correlation function, divided by its value at zero lag ( $q = 0$ ), drops below a certain threshold  $x$  [49]. Mathematically, it can be expressed as follows:

$$B_c(x) = \min\left\{\Delta f : \left| \frac{R_{\text{HH}}(q)}{R_{\text{HH}}(0)} \right| < x\right\}. \quad (12)$$

Fig. 7(a)–(c) displays the coherence bandwidth at the correlation levels of 0.5, 0.7, and 0.9, respectively. It can be seen that the  $B_c$  has a behavior inversely proportional to the rms delay spread. Furthermore, the results indicate a significant dispersion of the calculated  $B_c$  inside the URA for most transmitter positions. However, this dispersion is considerably smaller for the  $B_c(0.9)$ . The same pattern is observed for both LOS and NLOS measurements. Nevertheless, the range of variation in NLOS cases is smaller.

Fig. 8 provides an overview of the behavior of  $B_c$  across the three correlation levels, along with a comparison of the cdfs. The 90% of the  $B_c$  were below 106, 63.3, and 18.6 MHz for the 0.5, 0.7, and 0.9 correlation levels, respectively. It can be noticed that there is no convergence between the three cdf curves which means that the  $B_c$  is highly dependent on the correlation level.

Table III presents a summary of the most significant  $B_c$  values observed for each correlation level. The results indicate that the minimum coherence bandwidth values, observed across the scenarios or samples, are from 0.67 to 7.3 MHz, while the maximum values ranged from 37.3 to 133.3 MHz. Similarly, the median coherence bandwidth values are shown from 8.67 to 77 MHz.

Therefore, it is important to determine which degree of correlation should be required to consider the channel effectively flat fading during  $B_c$ , as it reduces the fading and enhances the data transmission capacity which is crucial for high-data-rate communication systems.

## V. MASSIVE MU-MIMO MODEL AND SUM-RATE CAPACITY

### A. Massive MU-MIMO Channel Model

Assuming a simple uplink massive MU-MIMO system that is equipped with  $N_R$  antennas at the base station, which can support up to  $N_T$  active users in direct LOS. Each user

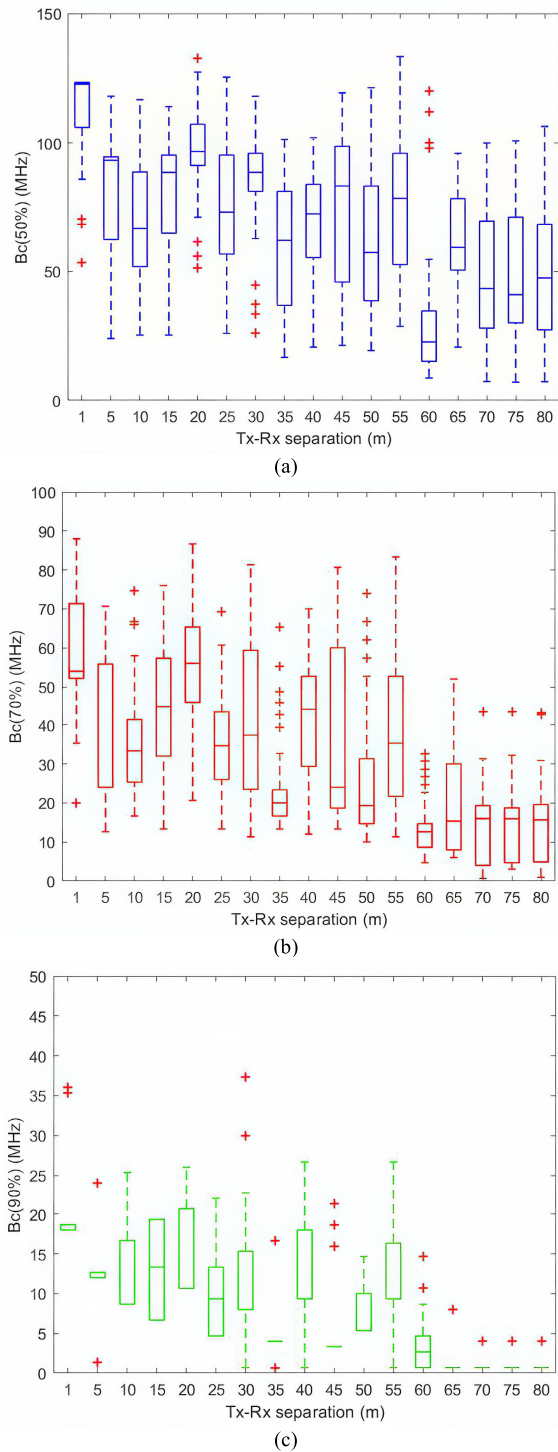


Fig. 7. Coherence bandwidth at different correlation levels: (a) 50%, (b) 70%, and (c) 90%.

transmits a total power of  $P$ , while the base station has channel knowledge, and the user terminals are not collaborating with each other. The system operates using an orthogonal frequency division multiplexing (OFDM) technique with  $N_f$  subcarriers that correspond to the measured tones. In this model, the received signal at the base station is developed for the  $k$ th subcarrier while  $N_t$  users are active

$$y[k] = H[k] \cdot x[k] + n[k]; \quad k = 1, 2, \dots, N_f \quad (13)$$

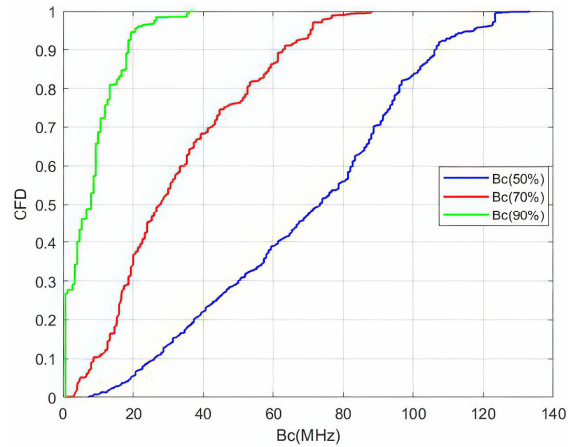


Fig. 8. Normalized PDPs measured from Rx25 at 1 and 40 m.

TABLE III  
SIGNIFICANT VALUES OF COHERENCE BANDWIDTH

C. level (%)	$B_c$ (min)	$B_c$ (max)	$B_c$ (median)
50	7.3	133.3	77
70	0.67	88	30.67
90	0.67	37.3	8.67

where  $x[k]$  and  $y[k]$  are the transmitted and received signal vectors at the  $k$ th subcarrier,  $H[k]$  is the  $N_R \times N_T$  normalized channel matrix, and  $n[k]$  is the zero-mean complex Gaussian noise vector with unit variance.

### B. Singular Value Spread

Massive MU-MIMO has the potential to separate users and make all spatial modes useful by utilizing a large number of antennas at the base station [10]. However, this depends on the availability of “favorable” propagation conditions, where the user channels become increasingly orthogonal with the increasing number of antennas. The assumption of such favorable propagation is often made in theoretical studies that rely on i.i.d. Rayleigh channels [10]. It is important to investigate the extent to which real massive MU-MIMO channels exhibit such favorable conditions. To assess the joint orthogonality of all users, one way is to analyze the SVS [50]. SVS is a metric used to evaluate the joint orthogonality of all users in real massive MIMO channels. The normalized propagation matrix has a singular value decomposition

$$H = U \Sigma V^H \quad (14)$$

where  $U$  and  $V$  are unitary matrices and  $\Sigma$  is a diagonal matrix that contains singular values of the channel  $\sigma_i$ ,  $i = 1, \dots, N_T$ . The SVS  $\kappa$  is then defined as follows:

$$\kappa = \frac{\max \sigma_i}{\min \sigma_i}. \quad (15)$$

Therefore, the SVS is within the range of 1 to infinity. A  $\kappa$  value closer to 1 implies almost complete user orthogonality (favorable propagation condition), while higher  $\kappa$  values suggest a significant linear dependence of at least two rows in the matrix  $H$  (unfavorable propagation condition).

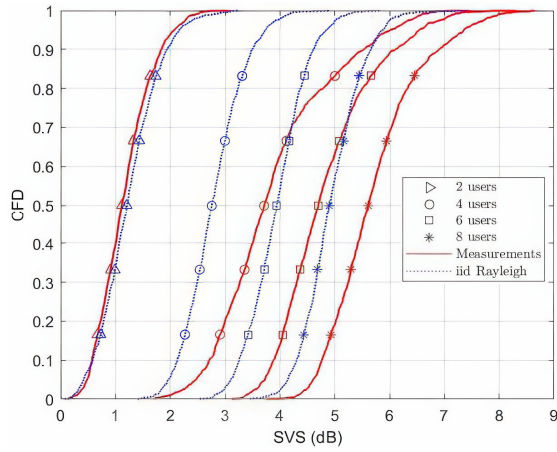


Fig. 9. cdfs of SVSs (dB) when using two, four, six, and eight users.

This dependence makes it challenging to separate the corresponding users spatially.

In Fig. 9, the cdf of the SVS is shown for the underground mine channel and i.i.d. Rayleigh channels with varying numbers of active users. It is observed that for i.i.d. Rayleigh channel, as the number of active users increases from 2 to 8, the median of the SVS gradually increases from 1.21 to 4.9 dB. Similarly, for the underground mine channel, the trends are comparable to those observed for i.i.d. Rayleigh channel. As the number of antennas increases from 2 to 8, the median of the SVS also increases from 1.11 to 5.9 dB.

Compared to i.i.d. Rayleigh channels, the measured channels exhibit a slightly higher SVS for four, six, and eight users. It is worth mentioning that when there are eight users, we could experience either favorable or unfavorable propagation conditions due to the SVS ranging from 3.74 to 8.64 dB. However, when fewer users are employed, the user orthogonality improves, bringing the curves closer to those of the i.i.d. Rayleigh channels.

### C. Sum-Rate Capacity

Capacity is a fundamental metric for evaluating wireless propagation channels, representing the maximum rate at which information can be transmitted without error. One prospect of massive MIMO systems is the relationship between receiver spatial correlation and sum-rate capacity. In fact, the sum capacity is a direct measure of channel quality, enabling a precise evaluation of its effectiveness. To calculate the sum capacity of the massive MU-MIMO-OFDM system, it is assumed that the base station has perfect knowledge of the channel. Therefore, the channel capacity can be expressed as follows [51]:

$$C = \log_2 \det \left[ I_{N_R} + \frac{\rho}{N_T} \mathbf{H}\mathbf{H}^* \right] \quad (16)$$

where  $I_{N_R}$  is the real identity matrix,  $\rho$  is the signal-to-noise ratio (SNR) at the Rx side, and  $\mathbf{H}$  is the normalized channel matrix.

As the number of receiving antennas  $N_R$ , increases toward infinity under favorable propagation conditions, and with a fixed number of transmitters  $N_T$ , the capacity of the up-link

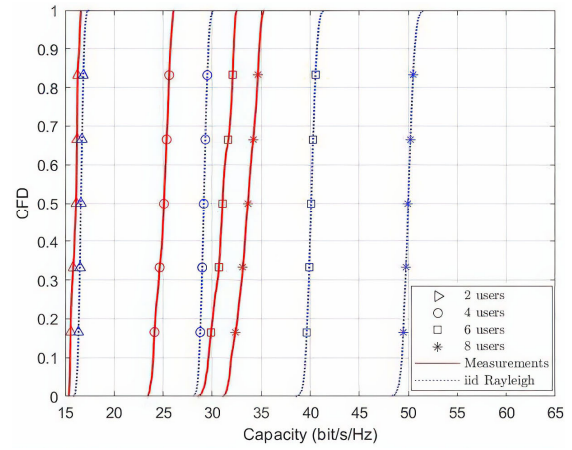


Fig. 10. cdfs of the sum-rate capacity for different number of users at an SNR of 10 dB.

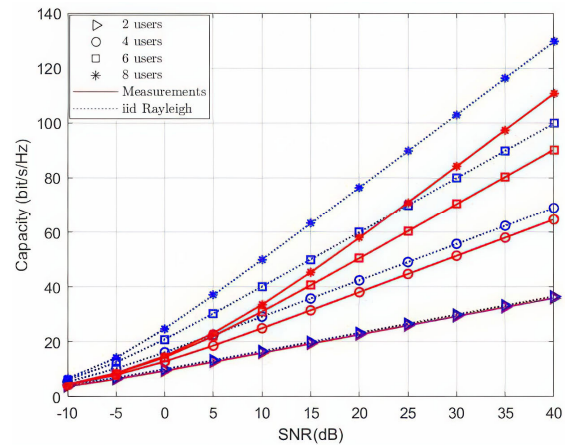


Fig. 11. Mean capacity at different SNRs and different number of users.

channel will approach an upper bound in an asymptotic manner [52]

$$C_b = N_T \log_2 \left( 1 + \frac{N_R}{N_T} \rho \right). \quad (17)$$

In Fig. 10, the cdf of the sum-rate capacity is presented for the underground mine environment, along with the i.i.d. Rayleigh channel cases. The SNR was fixed to 10 dB, and the number of active users varied from 2 to 8. The results indicate that the capacity increases as the number of active users increases for both the experimental and the i.i.d. Rayleigh channels. However, the measured capacities are lower than those corresponding to the i.i.d. channel. Moreover, as the number of active users increases, the difference between the measured capacities and those of the i.i.d. Rayleigh channel also increases. Furthermore, the figure shows that the throughput gains, when moving from two users to eighth users, are approximately 17.5 and 33.4 bit/s/Hz for the underground mine channel and i.i.d. Rayleigh channel, respectively.

Fig. 11 shows the uplink average capacity at different SNR values for varying numbers of users, along with the corresponding i.i.d. Rayleigh channel cases. It can be observed that as the number of users increases, there is a significant difference in channel capacity compared to the Rayleigh

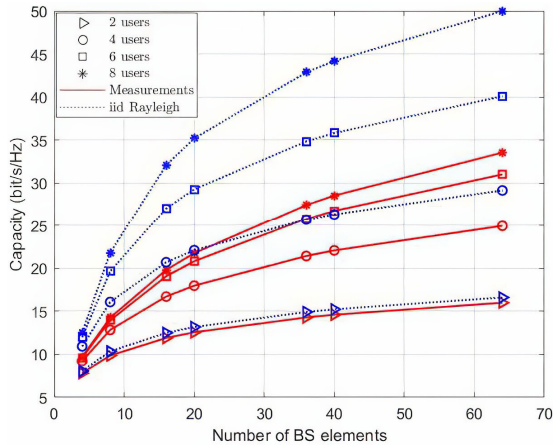


Fig. 12. Sum-rate capacity for different number of BS elements and users.

TABLE IV

MASSIVE MIMO CAPACITY IMPROVEMENT IN VARIOUS CHANNELS

Ref.	Freq.	Environment	SNR	M. MIMO	Improv. in C
[53]	3.2 – 4 GHz	Conference room	10	100x20	89%
[44]	3.5 GHz (200 MHz)	Outdoor	20	16x256	73%
This work	28 GHz (800 MHz)	Underground mine	10	8x64	67%
[54]	3.5GHz (160 MHz)	Shanghai subway tunnel	10	32x64	62%

channel cases. In the case of eight users, the channel reaches a capacity of 67% with respect to an i.i.d. Rayleigh channel, which for an SNR of 10 dB is 33.54 bits/s/Hz. The difference between measured and i.i.d. Rayleigh channel can be explained by the increasing similarity between multipaths as the propagation distance increases, thereby reducing the ability of channel diversity gain. Additionally, as the SNR increases, the channel is found to achieve capacities of more than 80% with respect to i.i.d. Rayleigh channels.

Fig. 12 displays the mean value of the capacity for various numbers of users as the number of antennas at the base station increases from 4 to 64, including cases with i.i.d. Rayleigh channels. The results reveal that the capacity is positively correlated with the number of antennas at the BS. By comparing a conventional  $8 \times 4$  MU-MIMO with an  $8 \times 64$  massive MU-MIMO, it can be seen that the mean capacity has increased from 9.69 to 33.54 bits/s/Hz. This indicates that massive MIMO provides better performance than conventional MIMO. Additionally, when the number of users is fixed, the capacity of the up-link channel will converge to an upper limit as the number of BS antennas increases.

Table IV presents a comprehensive comparison of capacity improvements across different types of channels. It summarizes the capacity improvement relative to the i.i.d. Rayleigh channel in various environments, showcasing the impact of massive MIMO.

From Table IV, it can be observed that the conference room showed the most substantial improvement, followed by the

outdoor channel, our underground mine, and the Shanghai subway tunnel. These differences in improvement are attributed to channel characteristics. In tunnel-like environments (subway tunnel and underground mine), as the Tx–Rx separation distance increases, the correlation between multipath components increases as well, leading to a reduced diversity gain. In contrast, conventional indoor and outdoor environments have lower multipath correlation due to the varied propagation paths, reflections, and obstacles present in these settings, contributing to the diversity of signal paths and, consequently, resulting in greater capacity gains. The underground mine demonstrates a greater capacity improvement compared to the subway tunnel due to the irregularity of the mining gallery and the roughness of its walls, both of which facilitate scattering and reduce the similarity among multipath components. Therefore, while massive MIMO enhances capacity, the extent of improvement varies with channel characteristics, with tunnels showing lower gains due to increased multipath correlation compared to conventional environments.

## VI. SUMMARY AND CONCLUSION

This study investigates the characteristics of a massive MU-MIMO channel at 28 GHz in an underground gold mine. Radio channel measurements and performance analysis are conducted to better understand the behavior of the channel in this unique propagation environment that requires specialized examination. The analysis findings demonstrate a strong correlation between the propagation characteristics and the underground mine environment. Path loss measurements indicate a waveguiding effect in the mining gallery, particularly after a specific break point distance. This characteristic improves the received signal power at mmWaves, offering significant advantages for long-distance communication while reducing the need for extensive communications infrastructure. In comparison to the standard log-distance path loss model, the multislope path loss model is more appropriate for effectively characterizing all possible propagation mechanisms across different underground mine gallery segments. The time dispersion analysis reveals that mine galleries do not produce a significant time dispersion which leads to a higher signal quality and lower error rates in data transmission. Moreover, the rms delay spread exhibits minimal correlation with distance due to the increased attenuation of mmWave caused by scattering and reflections. The coherence bandwidth was also investigated at different correlation levels, and the results showed very scattered values among the 64 sub-channels established between a specific user and the BS. Finally, the sum-rate capacity was investigated with respect to the reference i.i.d. Rayleigh channel, and it was found to reach a capacity of 67%. The difference between the measured and i.i.d. Rayleigh channel is because the former contains multipath components that are highly similar. However, compared to the conventional MIMO system, the channel capacity has been greatly improved, which for a fixed SNR of 10 dB has increased from 9.69 to 33.54 bits/s/Hz. Consequently, it can be concluded that massive MU-MIMO technology has the potential to significantly improve the performance of mmWave signals inside underground mine environments.

## REFERENCES

- [1] J. Lööv, L. Abrahamsson, and J. Johansson, "Mining 4.0—The impact of new technology from a work place perspective," *Mining, Metall. Exploration*, vol. 36, no. 4, pp. 701–707, Aug. 2019, doi: 10.1007/s42461-019-00104-9.
- [2] S. M. Riurean, M. Leba, and A. C. Ionica, "Conventional and advanced technologies for wireless transmission in underground mine," in *Application of Visible Light Wireless Communication in Underground Mine*. Cham, Switzerland: Springer, 2021, pp. 41–125.
- [3] M. Jadoul. (2021). *Here is Why Mining is Digging Into 5G*. [Blog] NOKIA. [Online]. Available: <https://www.nokia.com/blog/here-is-why-mining-is-digging-into-5g/>
- [4] M. Ghaddar, I. Ben Mabrouk, M. Nedil, K. Hettak, and L. Talbi, "Deterministic modeling of 5G millimeter-wave communication in an underground mine tunnel," *IEEE Access*, vol. 7, pp. 116519–116528, 2019.
- [5] O. Kolade and L. Cheng, "Markov model characterization of a multicarrier narrowband powerline channel with memory in an underground mining environment," *IEEE Access*, vol. 9, pp. 59085–59092, 2021.
- [6] R. Flamini et al., "Toward a heterogeneous smart electromagnetic environment for millimeter-wave communications: An industrial viewpoint," *IEEE Trans. Antennas Propag.*, vol. 70, no. 10, pp. 8898–8910, Oct. 2022.
- [7] T. S. Rappaport, G. R. MacCartney, M. K. Samimi, and S. Sun, "Wideband millimeter-wave propagation measurements and channel models for future wireless communication system design," *IEEE Trans. Commun.*, vol. 63, no. 9, pp. 3029–3056, Sep. 2015.
- [8] G. R. Maccartney, T. S. Rappaport, S. Sun, and S. Deng, "Indoor office wideband millimeter-wave propagation measurements and channel models at 28 and 73 GHz for ultra-dense 5G wireless networks," *IEEE Access*, vol. 3, pp. 2388–2424, 2015.
- [9] J.-Y. Lee, J.-H. Lee, and S.-C. Kim, "Improving the accuracy of millimeter-wave ray-tracing simulations by modeling roadside trees," *IEEE Antennas Wireless Propag. Lett.*, vol. 18, no. 1, pp. 162–166, Jan. 2019.
- [10] X. Gao, O. Edfors, F. Rusek, and F. Tufvesson, "Massive MIMO performance evaluation based on measured propagation data," *IEEE Trans. Wireless Commun.*, vol. 14, no. 7, pp. 3899–3911, Jul. 2015.
- [11] S. Mumtaz, J. Rodriguez, and L. Dai, "mmWave Massive MIMO: A Paradigm for 5G. New York, NY, USA: Academic, 2016.
- [12] J. Huang, C.-X. Wang, R. Feng, J. Sun, W. Zhang, and Y. Yang, "Multi-frequency mmWave massive MIMO channel measurements and characterization for 5G wireless communication systems," *IEEE J. Sel. Areas Commun.*, vol. 35, no. 7, pp. 1591–1605, Jul. 2017.
- [13] M. Shafi et al., "5G: A tutorial overview of standards, trials, challenges, deployment, and practice," *IEEE J. Sel. Areas Commun.*, vol. 35, no. 6, pp. 1201–1221, Jun. 2017.
- [14] S. A. M. Tariq, C. L. Despina, S. Affes, and C. Nerguizian, "Angular dispersion of a scattered underground wireless channel at 60 GHz," *IEEE Access*, vol. 8, pp. 67572–67580, 2020.
- [15] S. Singh, F. Ziliotto, U. Madhow, E. Belding, and M. Rodwell, "Blockage and directivity in 60 GHz wireless personal area networks: From cross-layer model to multihop MAC design," *IEEE J. Sel. Areas Commun.*, vol. 27, no. 8, pp. 1400–1413, Oct. 2009.
- [16] M. El Khaled, P. Fortier, and M. L. Ammari, "A performance study of line-of-sight millimeter-wave underground mine channel," *IEEE Antennas Wireless Propag. Lett.*, vol. 13, pp. 1148–1151, 2014.
- [17] M. Ghaddar, L. Talbi, M. Nedil, I. Ben Mabrouk, and T. A. Denidni, "Mm-waves propagation measurements in underground mine using directional MIMO antennas," *IET Microw., Antennas Propag.*, vol. 10, no. 5, pp. 517–524, Apr. 2016.
- [18] H. Wei, G. Zheng, and M. Jia, "The measurements and simulations of millimeter wave propagation at 38ghz in circular subway tunnels," in *Proc. China-Jpn. Joint Microw. Conf.*, Sep. 2008, pp. 51–54.
- [19] A. González-Plaza, C. Calvo-Ramírez, C. Briso-Rodríguez, J. Moreno García-Loygorri, D. Oliva, and J. I. Alonso, "Propagation at mmW band in metropolitan railway tunnels," *Wireless Commun. Mobile Comput.*, vol. 2018, pp. 1–10, Mar. 2018.
- [20] X. Liu, X. Yin, and G. Zheng, "Experimental investigation of millimeter-wave MIMO channel characteristics in tunnel," *IEEE Access*, vol. 7, pp. 108395–108399, 2019.
- [21] C. Wang, W. Ji, G. Zheng, and A. Saleem, "Analysis of propagation characteristics for various subway tunnel scenarios at 28 GHz," *Int. J. Antennas Propag.*, vol. 2021, pp. 1–16, Sep. 2021.
- [22] G. Yue, D. Yu, H. Qiu, K. Guan, L. Yang, and Q. Lv, "Measurements and ray tracing simulations for non-line-of-sight millimeter-wave channels in a confined corridor environment," *IEEE Access*, vol. 7, pp. 85066–85081, 2019.
- [23] Q. Song, P. Tang, T. Jiang, L. Tian, J. Zhang, and J. Dou, "Modeling of path loss characteristics in a waveguide-like structure scenario at 28 GHz," in *Proc. 15th Eur. Conf. Antennas Propag. (EuCAP)*, Dusseldorf, Germany, Mar. 2021, pp. 1–5.
- [24] Q. P. Soo et al., "Propagation measurement of a pedestrian tunnel at 24 GHz for 5G communications," *IEEE Access*, vol. 9, pp. 149934–149942, 2021.
- [25] J. Vehmas, J. Jarvelainen, S. L. H. Nguyen, R. Naderpour, and K. Haneda, "Millimeter-wave channel characterization at Helsinki airport in the 15, 28, and 60 GHz bands," in *Proc. IEEE 84th Veh. Technol. Conf. (VTC-Fall)*, Montreal, QC, Canada, Sep. 2016, pp. 1–5.
- [26] M. Khatun, C. Guo, L. Moro, D. Matolak, and H. Mehrpouyan, "Millimeter-wave path loss at 73 GHz in indoor and outdoor airport environments," in *Proc. IEEE 90th Veh. Technol. Conf. (VTC-Fall)*, Honolulu, HI, USA, Sep. 2019, pp. 1–5.
- [27] S. Li, Y. Liu, L. Lin, and Q. Sun, "Measurements and characterization for millimeter-wave massive MIMO channel in high-speed railway station environment at 28 GHz," *Int. J. Antennas Propag.*, vol. 2021, pp. 1–15, Oct. 2021.
- [28] I. Ben Mabrouk, J. Hautcoeur, L. Talbi, M. Nedil, and K. Hettak, "Feasibility of a millimeter-wave MIMO system for short-range wireless communications in an underground gold mine," *IEEE Trans. Antennas Propag.*, vol. 61, no. 8, pp. 4296–4305, Aug. 2013.
- [29] X. Yin, X. Liu, G. Zheng, A. Saleem, and X. Zhai, "28-GHz channel characterization for a short tunnel," *IEEE Microw. Wireless Compon. Lett.*, vol. 28, no. 12, pp. 1146–1148, Dec. 2018.
- [30] X. Yin, G. Zheng, and A. Saleem, "Influence of antenna configuration on mm-wave MIMO performance in a subway-like tunnel," *IET Microw., Antennas Propag.*, vol. 12, no. 15, pp. 2395–2401, Dec. 2018.
- [31] L. Rubio et al., "Millimeter wave channel measurements in an intrawagon environment," *IEEE Trans. Veh. Technol.*, vol. 68, no. 12, pp. 12427–12431, Dec. 2019.
- [32] F. Challita et al., "On the contribution of dense multipath components in an intrawagon environment for 5G mmW massive MIMO channels," *IEEE Antennas Wireless Propag. Lett.*, vol. 18, no. 12, pp. 2483–2487, Dec. 2019.
- [33] Y. Shen, Y. Shao, L. Xi, H. Zhang, and J. Zhang, "Millimeter-wave propagation measurement and modeling in indoor corridor and stairwell at 26 and 38 GHz," *IEEE Access*, vol. 9, pp. 87792–87805, 2021.
- [34] *Decision on Releasing Millimetre Wave Spectrum to Support 5G*, document SLPB-003-19, Innovation, Science and Economic Development Canada, 2019. [Online]. Available: <https://www.ic.gc.ca/eic/site/smt-gst.nsf/vwapj/SLPB-003-19EN.pdf/file/SLPB-003-19EN.pdf>
- [35] J. R. Pérez et al., "Empirical characterization of the indoor radio channel for array antenna systems in the 3 to 4 GHz frequency band," *IEEE Access*, vol. 7, pp. 94725–94736, 2019.
- [36] Anritsu. (2013). *Time Domain Measurements Using Vector Network Analyzers MS4640 Series*. [Online]. Available: <https://dl.cdn-anritsu.com/en-us/test-measurement/files/Application-Notes/Application-Note/11410-00722A.pdf>
- [37] R. Nilsson, "Analysis of path-losses along the Kankberg tunnel with comparisons between LTE measurements and radio-channel measurements: A report to the PIMM project," Luleå Univ. Technol., Sweden, Tech. Rep., 2017. [Online]. Available: [www.ltu.se](http://www.ltu.se)
- [38] C.-Y. Wu et al., "Distributed multi-user MIMO transmission using real-time sigma-delta-over-fiber for next generation fronthaul interface," *J. Lightw. Technol.*, vol. 38, no. 4, pp. 705–713, Feb. 2020.
- [39] Z. El Khaled, W. Ajib, and H. Mcheick, "Log distance path loss model: Application and improvement for sub 5 GHz rural fixed wireless networks," *IEEE Access*, vol. 10, pp. 52020–52029, 2022.
- [40] C. Briso-Rodríguez, P. Fratilescu, and Y. Xu, "Path loss modeling for train-to-train communications in subway tunnels at 900/2400 MHz," *IEEE Antennas Wireless Propag. Lett.*, vol. 18, no. 6, pp. 1164–1168, Jun. 2019.
- [41] I. Ben Mabrouk, L. Talbi, M. Nedil, and K. Hettak, "MIMO-UWB channel characterization within an underground mine gallery," *IEEE Trans. Antennas Propag.*, vol. 60, no. 10, pp. 4866–4874, Oct. 2012.
- [42] Y. P. Zhang, "Novel model for propagation loss prediction in tunnels," *IEEE Trans. Veh. Technol.*, vol. 52, no. 5, pp. 1308–1314, Sep. 2003.

- [43] S. Li, Y. Liu, L. Yao, and W. Cao, "Improved channel model and analysis of the effect of bodies in curved tunnel using ray tracing," *IEEE Antennas Wireless Propag. Lett.*, vol. 19, no. 7, pp. 1162–1166, Jul. 2020.
- [44] Z. Hu, W. Ji, H. Zhao, X. Zhai, A. Saleem, and G. Zheng, "Channel measurement for multiple frequency bands in subway tunnel scenario," *Int. J. Antennas Propag.*, vol. 2021, pp. 1–13, Jun. 2021.
- [45] S. Deng, M. K. Samimi, and T. S. Rappaport, "28 GHz and 73 GHz millimeter-wave indoor propagation measurements and path loss models," in *Proc. IEEE Int. Conf. Commun. Workshop (ICCW)*, Jun. 2015, pp. 1244–1250.
- [46] T. S. Rappaport, *Wireless Communications: Principles and Practice*, vol. 2. Upper Saddle River, NJ, USA: Prentice-Hall, 1996.
- [47] M. Boutin, A. Benzakour, C. L. Despins, and S. Affes, "Radio wave characterization and modeling in underground mine tunnels," *IEEE Trans. Antennas Propag.*, vol. 56, no. 2, pp. 540–549, Feb. 2008.
- [48] G. Li et al., "Channel characterization for mobile hotspot network in subway tunnels at 30 GHz band," in *Proc. IEEE 83rd Veh. Technol. Conf. (VTC Spring)*, Nanjing, China, May 2016, pp. 1–5.
- [49] V. Kristem, C. U. Bas, R. Wang, and A. F. Molisch, "Outdoor wideband channel measurements and modeling in the 3–18 GHz band," *IEEE Trans. Wireless Commun.*, vol. 17, no. 7, pp. 4620–4633, Jul. 2018.
- [50] D. Gesbert, M. Shafi, D.-s. Shiu, P. J. Smith, and A. Naguib, "From theory to practice: An overview of MIMO space-time coded wireless systems," *IEEE J. Sel. Areas Commun.*, vol. 21, no. 3, pp. 281–302, Apr. 2003.
- [51] A. F. Molisch, M. Steinbauer, M. Toeltsch, E. Bonek, and R. S. Thoma, "Capacity of MIMO systems based on measured wireless channels," *IEEE J. Sel. Areas Commun.*, vol. 20, no. 3, pp. 561–569, Apr. 2002.
- [52] F. Rusek et al., "Scaling up MIMO: Opportunities and challenges with very large arrays," *IEEE Signal Process. Mag.*, vol. 30, no. 1, pp. 40–60, Jan. 2013.
- [53] J. R. Pérez, R. P. Torres, M. Domingo, L. Valle, and J. Basterrechea, "Analysis of massive MIMO performance in an indoor picocell with high number of users," *IEEE Access*, vol. 8, pp. 107025–107034, 2020.
- [54] J. Zhang, Z. Zheng, Y. Zhang, J. Xi, X. Zhao, and G. Gui, "3D MIMO for 5G NR: Several observations from 32 to massive 256 antennas based on channel measurement," *IEEE Commun. Mag.*, vol. 56, no. 3, pp. 62–70, Mar. 2018.



**Saif Eddine Hadji** (Member, IEEE) received the Dipl.Ing. degree from the Polytechnic School, Algiers, Algeria, in 2009, and the M.Sc. degree from the University of Technology Malaysia (UTM), Johor Bahru, Malaysia, in 2016, where he is currently pursuing the Ph.D. degree.

He is doing research at the University of Quebec in Abitibi-Témiscamingue, Val D'or, QC, Canada. His current research interests include wireless communication in underground mines, and artificial intelligence-based channel modeling.



**Mourad Nedil** (Senior Member, IEEE) received the Dipl.Ing. degree from the University of Algiers (USTHB), Algiers, Algeria, in 1996, the D.E.A. (M.S.) degree from the University of Marne la Vallée, Marne la Vallée, France, in 2000, and the Ph.D. degree from the Institut National de la Recherche Scientifique (INRS-EMT), Université de Québec, Montreal, QC, Canada, in 2006.

In June 2008, he joined the Engineering School Department, University of Quebec in Abitibi-Témiscamingue, Val D'or, QC, where he is currently a Full Professor. His research interests include antennas, multiple-input and multiple-output (MIMO) radio-wave propagation, and microwave devices.

Dr. Nedil received a Post-Doctoral Fellowship from INRS-EMT, RF Communications Systems Group, from 2006 to 2008.



**Mohamed Lamine Seddiki** received the Dipl.Ing. degree in telecommunication from the University of Blida, Ouled Yaïch, Algeria, in 2012, and the M.Sc. degree from the University of Quebec in Abitibi-Témiscamingue, Val D'or, QC, Canada, in 2017, where he is currently pursuing the Ph.D. degree.

His research interests include microwave components, microwave reconfigurable circuits, and multiple-input and multiple-output (MIMO) systems.



**Ismail Ben Mabrouk** (Senior Member, IEEE) received the B.A.Sc. and M.Sc. degrees in electrical engineering from the University of Lille, Lille, France, in 2006 and 2007, respectively, and the Ph.D. degree in electrical engineering from the University of Quebec, Montreal, QC, Canada, in 2012.

From 2007 to 2009, he was with Huawei Technologies, Paris, France. In 2012, he joined the Wireless Devices and Systems (WiDeS) Group, University of Southern California, Los Angeles, Los Angeles, CA, USA. He is currently an Assistant Professor with Durham University, Durham, U.K. His research interests include implantable and wearable antenna design, propagation studies for multiple-input and multiple-output (MIMO) systems at the millimeter-wave and THz frequencies, deep learning, and wireless body area network for medical applications.

Dr. Mabrouk was a recipient of the Abu Dhabi Award for Research Excellence (AARE).